Electronic Supplementary Material (ESI) for Chemical Science.
This journal is © The Royal Society of Chemistry 2023

Supporting Information

Caught in the act: real-time observation of the solvent response that promotes excited-state proton transfer in pyranine

Claudius Hoberg[1], **Justin J. Talbot**[2], **James Shee**[2], **Thorsten Ockelmann**[1], **Debasish DasMahanta**[1], **Fabio Novelli**[1], **Martin Head-Gordon**[2,3], and **Martina Havenith**[1]

[1]Lehrstuhl für Physikalische Chemie II, Ruhr-Universität Bochum, 44780 Bochum, Germany

[2]Kenneth S. Pitzer Center for Theoretical Chemistry, Department of Chemistry, University of California, Berkeley, California 94720, United States

[3]Chemical Sciences Division, Lawrence Berkeley National Laboratory, Berkeley, California, 94720, United States

Table of Contents

1 Experimental Fit of the OPTP Signals

As discussed in the main text, the time constants were obtained by fitting the OPTP traces to the following function

$$\frac{\Delta E}{E}(t) = S_{DH}(t) + S_{E_1}(t) + S_{E_2}(t), \tag{1}$$

where $S_{DH}(t)$ is a single damped harmonic oscillator describing the short-time signal ($t < 15$ ps) and a set of biexponential decay functions ($S_{E_1}(t), S_{E_2}(t)$) which describes the long-time response. The damped harmonic oscillator function used for the fit was

$$S_{DH}(t) = \frac{a_0}{\sqrt{\omega_0^2 - \delta^2}} e^{-\delta t} \sin t\sqrt{\omega_0^2 - \delta^2}, \tag{2}$$

where ω_0 and δ denotes the undamped angular frequency and the dampling constant, respectively. Specifically for HPTS, Eq. 2 can be simplified as a sum of two exponentially decaying terms

$$S_{DH}(t) = A_1 e^{-t/\tau_{DH_1}} + A_2 e^{-t/\tau_{DH_2}}, \tag{3}$$

where the exponential prefactors ($A_{1/2}$), and the time constants $\tau_{DH_{1/2}}$ are defined accordingly as

$$\tau_{DH_{1/2}} = \left(\delta \pm \sqrt{\delta^2 - \omega_0^2}\right)^{-1} \tag{4a}$$

$$A_{1/2} = \mp \frac{a_0}{2\sqrt{\delta^2 - \omega_0^2}}, \tag{4b}$$

which are obtained since an overdamped response is observed ($\delta > \omega_0$). In comparison, the

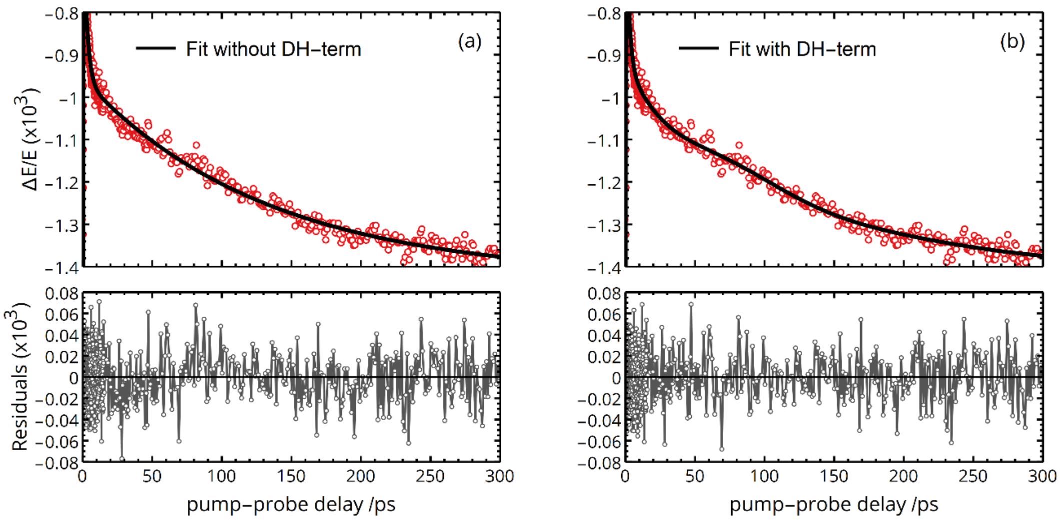

Fig. S1: A comparison of the different fit models for the OPTP data of HPTS with residuals. (a) Fit without the low-frequency damped harmonic oscillator term and (b) the fit with the low-frequency damped harmonic oscillator term.

damped harmonic oscillator fits for MPTS and OPTS reveal that an underdamped response is present in the OPTP signal.

The fitting was performed with Wolfram Mathematica 12.3 using the NonlinearModelFit function. The data points in the time interval 0.3-300 ps were included with the lower bound of 0.3 ps selected to account for the sharp signal at pump-probe overlap and to include only such points where the THz probe-pulse is separated in time from the optical pump-pulse. A comparison of the different fit models for HPTS, with and without $S_{DH}(t)$ is shown in Fig. S1. While the short time response is best fit to an overdamped harmonic oscillation, fitting with a damped harmonic oscillator function introduces a slight peak at $\approx$ 100 ps pump-probe delay time which resulted in a slightly lower residual. The results of the fit, including a full list of parameters, is provided in Table S1.

2 Static TDDFT Calculation Details

Linear-response time-dependent density functional theory (TDDFT) within the adiabatic approximation was employed to model the first-excited singlet state $S_1(\pi\pi*)$ of each system.

Table S1: Comparison of the fit parameters for HPTS solvated in H_2O and D_2O, MPTS, and OPTS. The fit includes the instantaneous response, the subsequent response described by an (over/under)damped harmonic oscillator, and the long-term exponential response.

	$a_0 \times 10^3$	ω_0/ps^{-1}	T/ps	δ/ps^{-1}	τ_1/ps	$a_1 \times 10^4$	τ_2/ps	$a_2 \times 10^4$	$\Delta E \times 10^3$
HPTS (H_2O)	1.75	1.52	4.1	2.6	5.4	0	120	5.6	-1.47
HPTS (D_2O)	1.95	1.59	4.0	2.3	9.6	3.3	150	6.1	-1.97
MPTS	0.43	1.58	4.0	0.7	5.4	3.1	120	1.4	-1.04
OPTS	0.70	1.91	3.3	0.5	5.4	1.7	120	0.5	-0.86

Table S2: A comparison between the measured experimental absorption and fluorescence energies and the calculated vertical excitation and emission energies. The use of state-specific non-equilibrium PCM yields a value of 2.40*.

	HPTS		MPTS		OPTS	
	Absorption	**Emission**	**Absorption**	**Emission**	**Absorption**	**Emission**
Exp. (eV)	3.07	2.82	2.72	2.43	3.08	2.88
Calc. (eV)	3.04	2.78	2.71	2.58*	3.06	2.78

The B3LYP/def2-SV(P) level of theory with an equilibrium PCM model led to calculated vertical excitation and emission energies that generally are in good agreement with the experimental absorption and fluorescence energies. Calculations of HPTS and OPTS include one explicit water molecule, while those of MPTS did not have an explicit water. As seen in Table S2, the calculated values agree remarkably well with the experimental measurements, suggesting this level of theory and basis set can adequately describe the ground and excited state electronic structure of the HPTS, MPTS, and OPTS molecules.

The calculations of the relaxation energy along the S_1 surface from the Franck-Condon region (corresponding to the optimized ground-state geometry) to the S_1 minimum – referred to in the main text as a Stokes shift – were performed as follows. Total energies in the Franck-Condon region were extracted from single-point TDDFT calculations. Total energies at the S_1 minima were extracted from the final iteration of excited-state geometry optimizations. All relevant quantities are shown in Table S3.

Attachment and detachment density plots (Fig. S2) reveal where electron density is

Table S3: Total energies involved in the Stokes shift calculations reported in the main text.

	E(S_1^{FC}) [Ha]	E(S_1^{min}) [Ha]	Δ E [kJ/mol]
HPTS	-3122.50228	-3122.516239	36.6
OPTS	-3122.05370	-3122.062376	22.8
MPTS	-3085.40751	-3085.418626	29.2

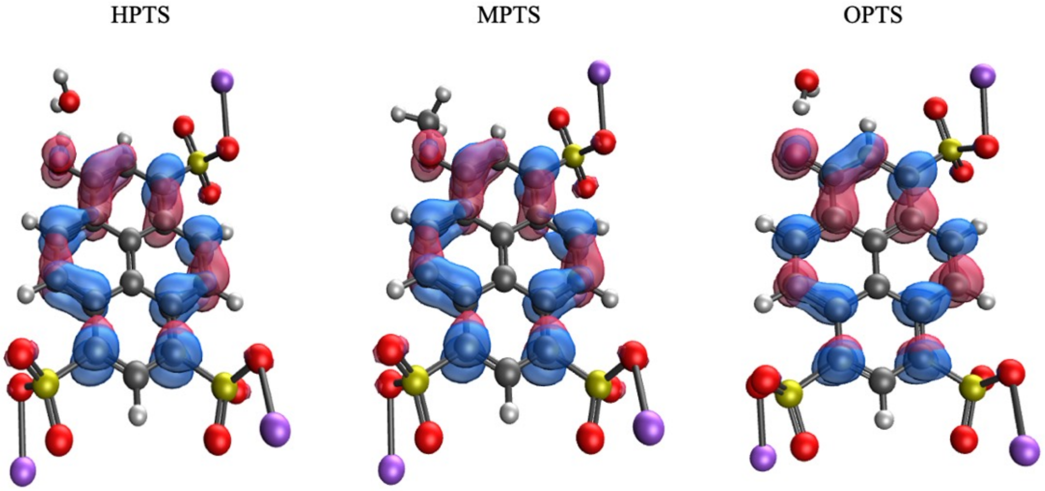

Fig. S2: Attachment (blue) and detachment (red) densities corresponding to the vertical excitation to the $S_1(\pi\pi^*)$ states in HPTS, MPTS, and OPTS.

added and removed upon vertical excitation from the ground- to first-excited singlet states. In all chromophores, the photoinduced electronic transition involves the removal of electron density from the lone pair in an oxygen p orbital and its redistribution into the π-system of the pyrene ring. This suggests a mesomeric effect in accordance with Baird's rule of (anti)aromaticity, which states that a cyclic aromatic molecule with $(4N+2)\pi$ electrons in its perimeter will be aromatic (and energetically stabilized) in the ground-state but anti-aromatic (and energetically destabilized) in the excited state. The charge rearrangement-induced relief of excited-state antiaromaticity thus contributes to the substantial Stokes shifts reported here for all three species and constitutes a driving force behind the observed energy transfer into the solvent environment. We note that this phenomenon has been shown in Ref. 1 to drive a number of other excited-state proton transfer processes.

3 Bilinearly-Coupled Harmonic Oscillator Model

Proton transfer is facilitated by the solvent rearrangements that result from vibrational energy being transferred between the chromophore and the water network. This can be simply modelled via a system of two bilinearly coupled harmonic oscillators [2] using the potential energy function

$$V(Q_{chr}, Q_{sol}) = \frac{1}{2} m_{chr} \omega_{chr}^2 Q_{chr}^2 + \frac{1}{2} m_{sol} \omega_{sol}^2 Q_{sol}^2 + c Q_{chr} Q_{sol}, \tag{5}$$

where Q_{chr} and Q_{sol} are single vibrational degrees of freedom on the chromophore and the solvent sub-systems respectively each with their respective reduced masses (m_{chr},m_{sol}) and harmonic frequencies (ω_{chr},ω_{sol}). The constant (c) denotes the bilinear coupling between the two oscillators. In this simplified model, complete energy transfer between the chromophore and solvent will occur when $m_{chr} = m_{sol} = m$ and $\omega_{chr} = \omega_{sol} = \omega$. In this unique case, the potential energy function can be expressed as

$$V(Q_{chr}, Q_{sol}) = \frac{1}{2} m \omega^2 (Q_{chr}^2 + Q_{sol}^2) + c Q_{chr} Q_{sol}. \tag{6}$$

The forces acting on each harmonic oscillator are given after applying Newton's second law

$$F_{chr} = m \frac{d^2 Q_{chr}}{dt^2} = -m\omega^2 Q_{chr} - c Q_{sol} \tag{7a}$$

$$F_{sol} = m \frac{d^2 Q_{sol}}{dt^2} = -m\omega^2 Q_{sol} - c Q_{chr} \tag{7b}$$

which introduce a coupled set of linear second-order differential equations of motion. Predicting vibrational energy transfer from the chromophore to the solvent requires constructing initial conditions for this set of differential equations that at time $t = 0$ the chromophore

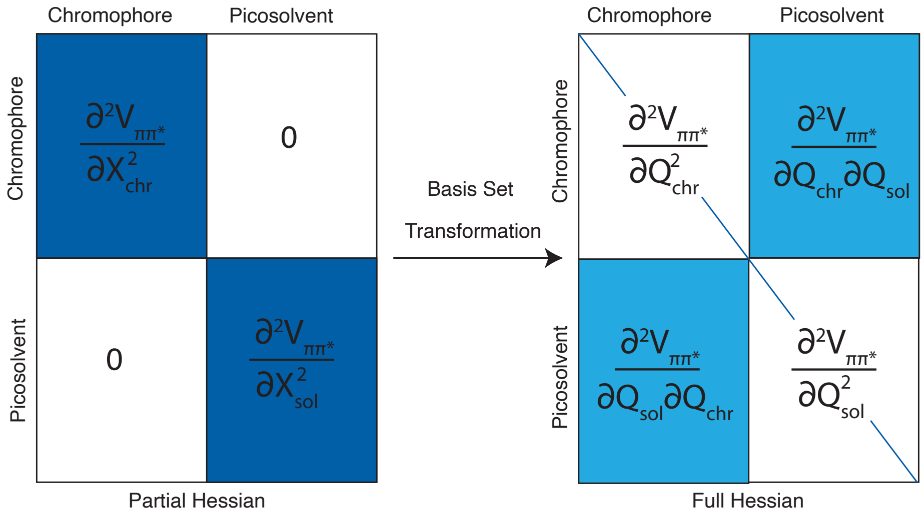

Fig. S3: Schematic diagram of the partial Hessian (left) employed to construct the basis set transformation that rotates the full Hessian onto fragment-localized mode basis (right).

mode is activated $Q_{chr}(0) = Q_0$ and the solvent mode is not $Q_{sol}(0) = 0$. The time dependence of the chromophore and solvent modes is

$$Q_{chr}(t) = Q_0 \cos\left(\frac{\omega_f + \omega_s}{2}t\right) \cos\left(\frac{\omega_f - \omega_s}{2}t\right) \tag{8a}$$

$$Q_{sol}(t) = Q_0 \cos\left(\frac{\omega_f + \omega_s}{2}t\right) \sin\left(\frac{\omega_f - \omega_s}{2}t\right) \tag{8b}$$

where $\omega_s = \sqrt{\omega^2 - \frac{c}{m}}$ and $\omega_f = \sqrt{\omega^2 + \frac{c}{m}}$ are now the coupled-mode frequencies that are split by the strength of the mass-weighted bilinear coupling constant. Since the zeroth-order harmonic oscillators are degenerate in this simplified model, the dynamics of Eq. 8 are a convoluted time signal where the difference frequency $(\omega_f - \omega_s)$ sets the rate of vibrational energy transfer.

The bilinearly-coupled harmonic oscillator model for two VDOF described above was adapted to include all vibrational degrees of freedom by fragment localizing the normal modes exactly onto the chromophore and picosolvent subsystems. As shown in Fig. S3, this required building a block-diagonal partial Hessian of the Cartesian second derivatives with respect to position (X_{chr}, X_{sol}). The eigenvectors of this partial Hessian matrix represent the fragment-localized VDOF which were employed to rotate the full Hessian matrix, i.e. the Hessian matrix that includes all second Cartesian derivatives, onto this basis. Localizing with this approach results in strictly no intra-fragment coupling between VDOF within each fragment, i.e. the chromophore-chromophore and picosolvent-picosolvent blocks of the full Hessian in this basis are diagonal, and inter-fragment coupling between the chromophore and picosolvent subsystems is potentially non-zero as represented by the off-diagonal blocks.

4 Additional Simulation Data

Fragment localizing the normal mode vibrational degrees of freedom results in a set of modes exactly localized on the chromophore and a set of modes exactly localized on the picosolvent. For reference, IQmol readable files (see Table S4) of the optimized coordinates and localized modes for each system are provided for download [3]. The harmonic frequencies (ν) in the region 1-6 THz are shown in Table S5. Interestingly, there is a systematic increase in the number of localized VDOF on both the chromophore and picosolvent subsystems going from HPTS to MPTS to OPTS, i.e. there are less chromophore and less picosolvent modes in the 1-6 THz region in HPTS then there are for MPTS or OPTS. However, in HPTS there are a few localized modes on the chromophore that are degenerate with picosolvent modes (e.g. chromophore modes Q_{33} and Q_{29} are degenerate with mircosolvent modes Q_{34} and Q_{28}, respectively). In comparison, amongst the harmonic frequencies in MPTS and OPTS there aren't any such degeneracies.

The representative beating frequencies (see Fig. 4 of the main text) between the chromophore and the picosolvent subsystems were calculated by Fourier transform of the population dynamics (see Eq. 9 of the main text) after initializing positions and momenta from a ground-state harmonic oscillator Wigner distribution. The molecular dynamics were performed in a similar manner to Ref. [4], except here the trajectories are classical harmonic oscillators. Sampling the Wigner distribution resulted in non-equilibrium positions

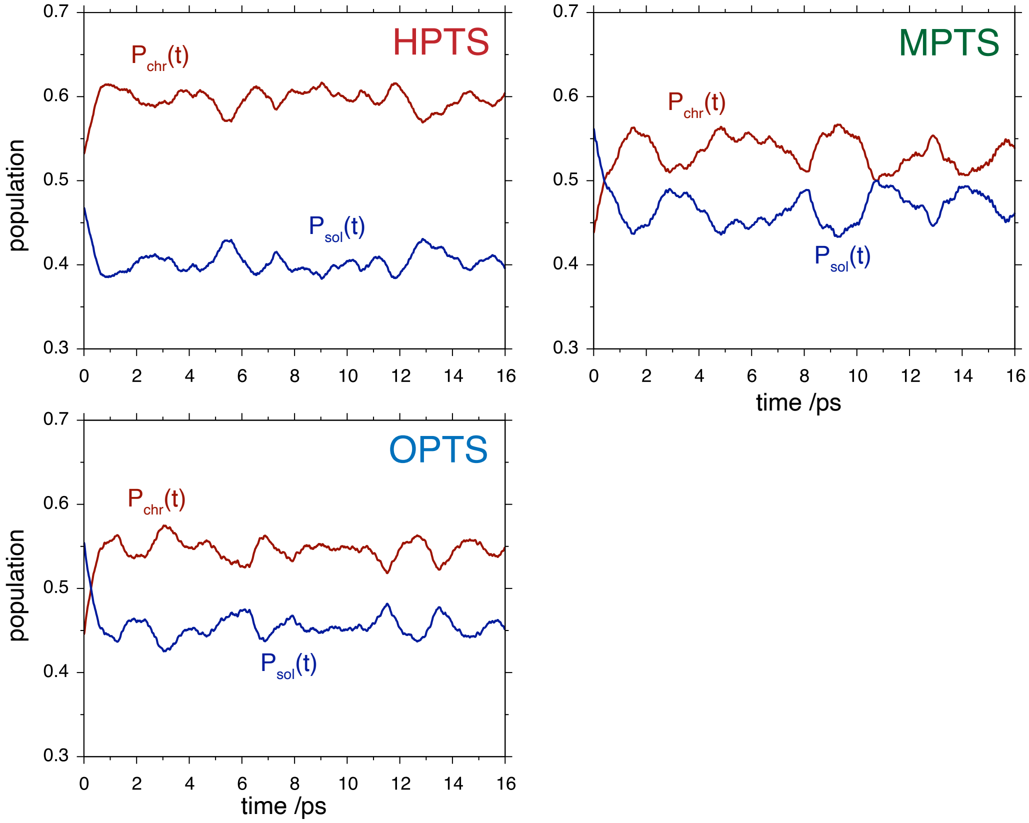

Fig. S4: Population transfer dynamics for HPTS, MPTS, and OPTS. The populations were calculated after sampling initial positions and momenta from the ground-state harmonic oscillator Wigner distribution of each chromophore-picosolvent cluster.

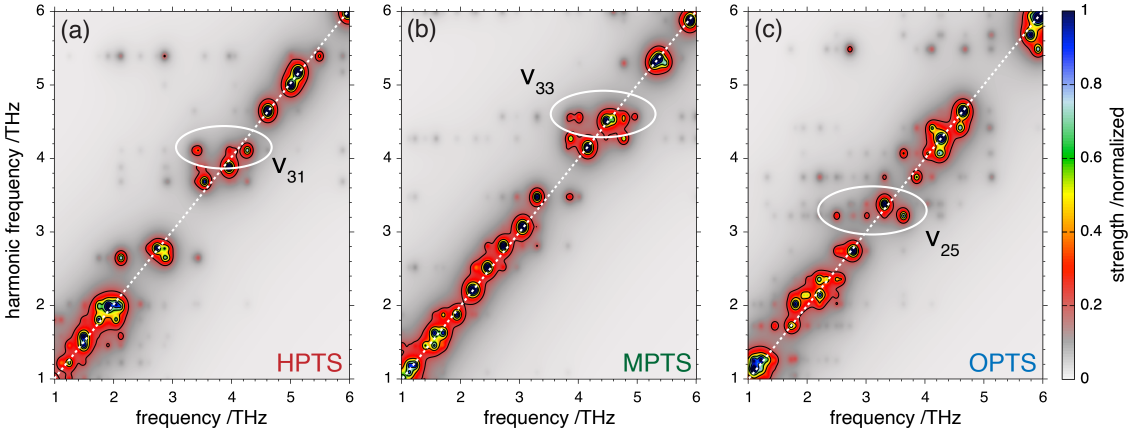

Fig. S5: Two-dimensional correlation maps of the harmonic frequency (ν from Table S5) of specific initialized fragment-localized chromophore modes as a function of the Fourier transformed frequencies (THz). the highlighted signatures (white circles) correspond to the fragment-localized modes shown in Fig. S6.

Table S4: A list of downloadable filenames containing the optimized geometries and IQmol readable fragment-localized harmonic frequency outputs.

Filename	Description
HPTS.8.xyz	S_0 and S_1 optimized geometries
HPTS.12.xyz	S_0 and S_1 optimized geometries
MPTS.8.xyz	S_0 and S_1 optimized geometries
OPTS.8.xyz	S_0 and S_1 optimized geometries
HPTS.8.out	S_1 Fragment-localized vibrational modes
HPTS.12.out	S_1 Fragment-localized vibrational modes
MPTS.8.out	S_1 Fragment-localized vibrational modes
OPTS.8.out	S_1 Fragment-localized vibrational modes

and momenta of the chromophore and picosolvent and, as a result, the trajectories were initialized with non-zero population in both subsystems. The initial time-averaged 16 ps of the population dynamics for each system are shown in Fig. S4. On average, the chromophore maintains $\approx 60\%$ of the population in HPTS compared with MPTS and OPTS which maintains $\approx 55\%$. As evident from the figure, the signal is comprised of low-frequency oscillations which required that the trajectories be run for 300 ps in order to get resolvable Fourier transforms. In a realistic simulation, with multiple solvent shells, the initial vibrational energy would dissipate into the bulk on these time scales.

The simplified schematics of the active VDOF shown in Fig. 6 of the main text were obtained from the single fragment-localized mode simulations. These simulations were initialized by populating single chromophore-localized modes, with the harmonic frequencies shown in Table S5, and Fourier transforming the resulting population dynamics after 300 ps. The maximum peak heights and strengths in the frequency domain were recorded and, in order to identify the signals clearly, the resulting spectra were artificially broadened by a two-dimensional Lorentzian function with a sharp 0.01 THz width. The results were then summed to give the two-dimensional correlation maps shown in Fig. S5. On the x-axis is the frequencies extracted from the Fourier transforms and on the y-axis is the harmonic frequency (ν) of the corresponding chromophore-localized mode. Since fragment-localization eliminates all intra-fragment coupling, i.e. the modes specific to each fragment

Table S5: A comparison between fragment-localized harmonic frequencies of the chromophore and picosolvent subsystems. All harmonic frequencies (ν) are reported in THz. The harmonic frequencies are sorted by fragment but otherwise ordered.

HPTS				MPTS				OPTS			
Chromophore		picosolvent		Chromophore		picosolvent		Chromophore		picosolvent	
#	ν	#	ν	#	ν	#	ν	#	ν	#	ν
9	1.01	10	1.12	11	1.09	13	1.42	8	1.04	10	1.15
11	1.22	13	1.53	12	1.19	15	1.56	9	1.13	13	1.33
12	1.46	15	1.77	14	1.46	17	1.70	11	1.25	14	1.47
13	1.58	19	2.14	16	1.63	19	2.01	12	1.27	16	1.92
16	1.81	20	2.48	18	1.88	20	2.18	15	1.72	18	2.04
17	1.98	21	2.60	21	2.21	23	2.70	17	2.02	21	2.40
18	2.02	24	2.94	22	2.52	25	3.01	19	2.14	22	2.50
22	2.65	25	3.18	24	2.81	28	3.69	20	2.36	23	2.70
23	2.78	26	3.40	26	3.07	29	4.06	24	2.74	26	3.35
27	3.69	28	3.88	27	3.48	34	4.65	25	3.22	28	3.48
29	3.88	30	4.10	30	4.15	35	4.92	27	3.38	29	3.55
31	4.11	34	5.00	31	4.27	38	5.42	30	3.75	32	4.12
32	4.65	-	-	32	4.51	39	5.69	31	4.07	35	4.47
33	5.00	-	-	33	4.57	40	5.84	33	4.28	36	4.56
35	5.17	-	-	36	5.30	-	-	34	4.42	38	5.12
36	5.39	-	-	37	5.36	-	-	37	4.65	39	5.32
37	5.98	-	-	41	5.88	-	-	41	5.49	40	5.43
-	-	-	-	42	6.00	-	-	42	5.68	43	5.71
-	-	-	-	-	-	-	-	45	5.91	44	5.82
-	-	-	-	-	-	-	-	46	5.95	-	-

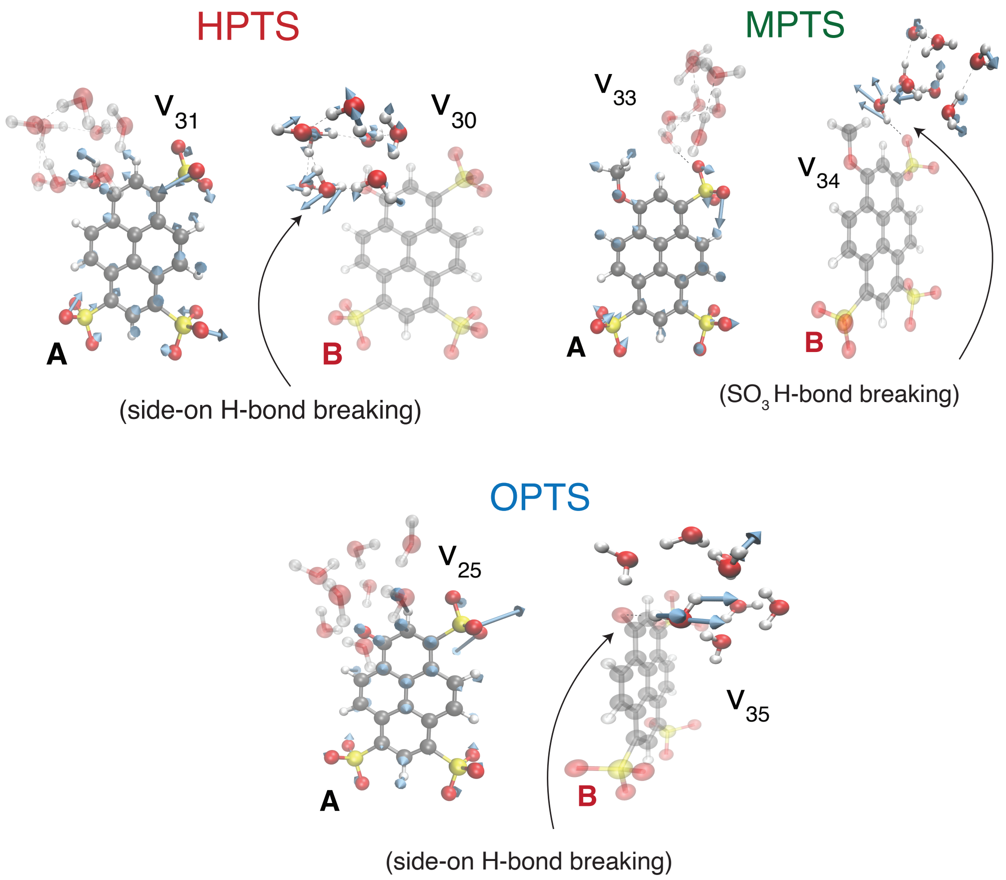

Fig. S6: The most active chromophore and picosolvent fragment-localized modes for HPTS, MPTS, and OPTS from the singly-initialized population dynamics trajectories. The mode numbers correspond to the harmonic frequencies in Table S5.

are uncoupled, THz signatures that are present off of the diagonal of the correlation plots correspond directly to chromophore modes that are directly coupled to the picosolvent.

In HPTS there are two correlated regions that have significant coupling (at a ≈ 4 THz and ≈ 3 THz). The ≈ 4 THz coupling (Q_{31}) corresponds to a symmetric skeletal bending motion of the chromophore with a side-on modulation of the picosolvent-chromophore hydrogen bond (see Fig. S6 with the resulting population dynamics shown in Fig. 6 of the main text). The most active vibrational energy transfer to the highlighted picosolvent mode (Q_{30}) is efficient for HPTS since the harmonic frequencies of these two modes are nearly degenerate (Q_{30} has a harmonic frequency of 4.11 THz for the chromophore mode and Q_{31} has a harmonic frequency of 4.10 THz for the picosolvent mode). The motion on

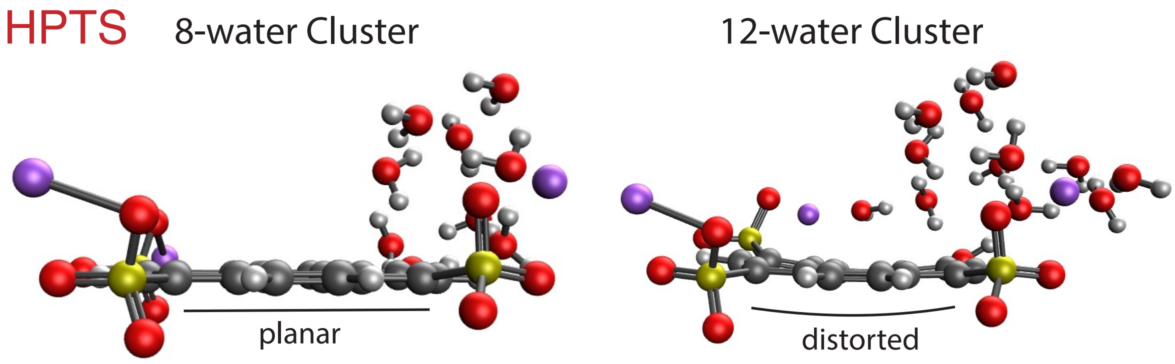

Fig. S7: A comparison between the optimized eight-water and the twelve-water chromophore-picosolvent clusters.

the chromophore in the 2.65 THz region corresponds to an out-of-plane rocking mode (Q_{22}) that modulates the side-on hydrogen bond in a similar way to the mode Q_{31}. Coupling to the picosolvent is less efficient in this region since the nearest solvent mode Q_{21} is 0.05 THz lower in frequency.

The correlation plots for MPTS and OPTS reveal less coupling to the picosolvent as evident by the mainly diagonal features in the low-frequency region. In MPTS, the minimum energy configuration of the picosolvent is clustered around the nearby SO_3 group and is much more disordered in comparison to HPTS. The correlation plot suggests that there is some coupling of the chromophore mode Q_{33} to the picosolvent mode Q_{34} as shown in Fig. S6—although the maximum amount of population transfer is only $\approx 20\%$. In OPTS, which appears to form a picosolvent geometry comparable to HPTS, the most significant coupling is between the chromophore mode (Q_{25}) and the picosolvent mode (Q_{35}) even though the harmonic frequencies of these two modes are split by 1.25 THz. While this may seem surprising, the in-plane hydrogen bond made with the picosolvent significantly *lowers* the frequency of the chromophore mode (Q_{25}) when compared to the similar mode in HPTS (Q_{31}).

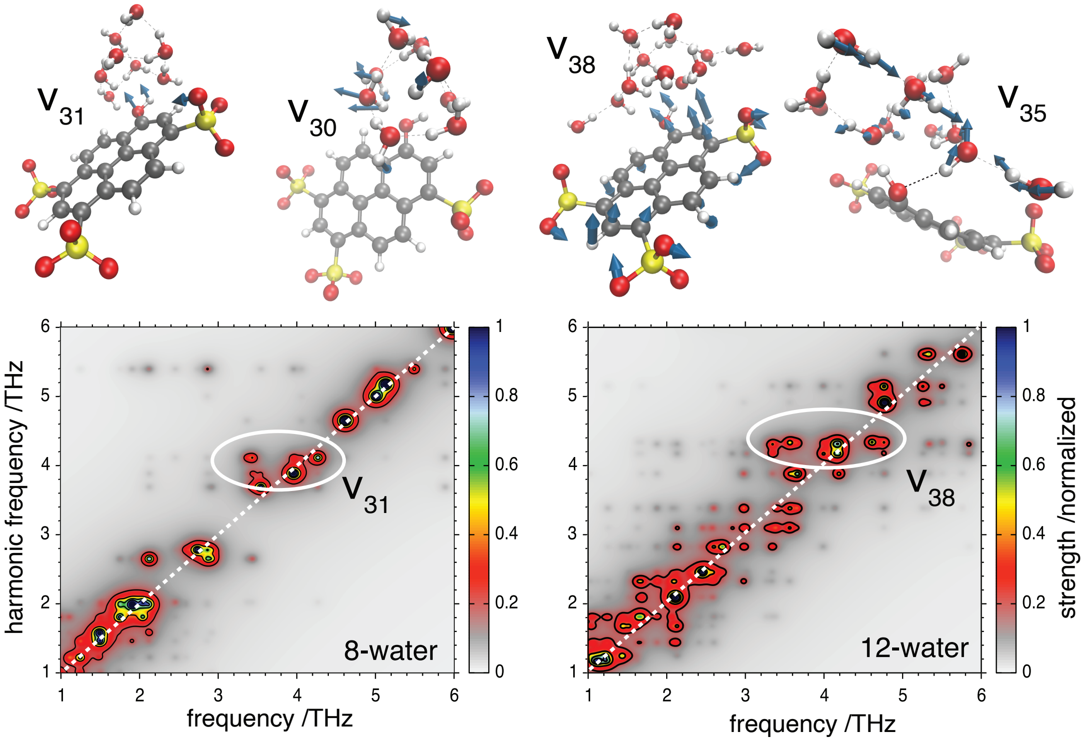

Fig. S8: A comparison between the correlation plots (bottom) of the eight water and twelve water HPTS clusters. The highlighted active modes are shown in the top panel.

5 Additional Convergence Tests

As discussed in the main text, additional convergence tests were performed on HPTS by increasing the number of water molecules from eight to twelve in the picosolvent. This resulted in a bending of the planar geometry of the chromophore, since the picosolvent is large enough to hydrogen bond with nearby SO_3 groups, when compared to the eight water cluster (see Fig. S7). Running the geometry optimizations with PCM was intended to correct for this and, while it appears to have done so in the eight water cluster, the twelve water cluster distorts and as a result an artificial mixing between in-plane and out-of-plane chromophore modes occurs. Clearly, this is an artifact of a reduced-size solvent as the fully-solvated chromophore is planar as it is isotropically solvated.

The simulated experiment where individual chromophore modes were initialized was also performed for the twelve water cluster in order to elucidate the coupled modes. In general,

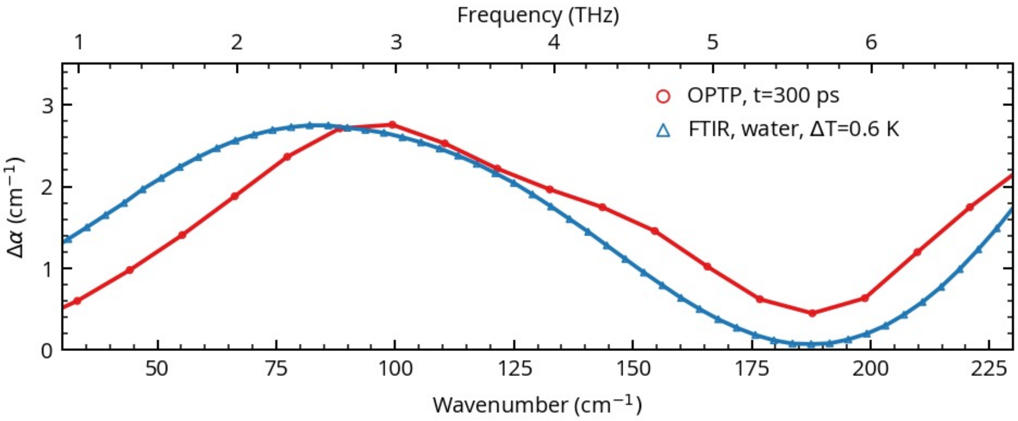

Fig. S9: Frequency-resolved OPTP spectrum of the HPTS solution at 300 ps after excitation (red) and the expected change in absorption for a temperature increase of $\Delta T = 0.6$K. Equilibrium far-infrared absorption data of water from Ref. 5.

there is more coupling between the chromophore and picosolvent in the twelve water cluster, compared with the eight water, as evident from the off-diagonal peaks in the correlation plots (see the bottom panel of Fig. S8). Although the planar structure of the chromophore is distorted in the twelve water cluster, there are active modes near $\approx$ 4 THz that are similar in motion to those of the eight water cluster as shown in the top panel of Fig. S8. The twelve water cluster has more motion on the skeletal backbone than in the eight water, however both have substantial motion on the OH group and the corresponding picosolvent mode in both systems has a substantial component that modulates the equatorial hydrogen bond. These results lead us to believe that the experimental signatures in the $\approx$ 4 THz region are derivative from these types of motions.

6 Estimation of Temperature Increase

To estimate the temperature increase, we compare the frequency-resolved OPTP signal at 300 ps with the equilibrium far-infrared absorption data of water [6]. Based on the equilibrium absorption data at 20.2°C and 0.4°C of Ref. 6, we calculate the expected absorption change for different temperature increases ΔT. We found a best match of the spectral OPTP response at 300 ps and the equilibrium FTIR data for a temperature difference of about $\Delta T = 0.6$K. In Fig. S9, we compare the OPTP spectrum at a pump-probe time delay of 300 ps with the absorption difference from the FTIR data. Both the OPTP spectrum and the equilibrium data show the same qualitative spectral shape with a minimum at ≈ 187 cm^{-1}, as well as a maximum around ≈ 75 to 100 cm^{-1}. We note that the OPTP data does not fully resemble the completely thermalized equilibrium data even at a delay of 300 ps.

7 Estimation of Heat Transport

For simplicity, we consider for the cell a cylindrical region of length l and radius b at temperature $T + \Delta T$ in contact with a thermal bath at temperature T. Here, we estimate the thermalization time by taking the length l as the sample thickness ($100 \mu m$). After the temperature change (ΔT) triggered by the pump excitation, the transmitted THz field is $E_{THz} + \Delta E_{THz}$, and after cooling it returns to E_{THz}. We expect the time dependence of ΔE_{THz} to track the time dependence of ΔT. The latter is described by a sum of exponential functions in time, keeping only the terms with the two largest relaxation times we have

$$\Delta T \approx C_2 e^{-t/\tau_2} + C_3 e^{-t/\tau_3} \tag{9a}$$

$$\tau_j = \frac{l^2}{\alpha_j^2 D_T} \tag{9b}$$

with $j = 2, 3$, C_2, C_3 are constants, α_2 and α_3 are, respectively, the two smallest roots of the equation $J_0(\alpha, \beta) = 0$ where J_0 is the Bessel function of the first kind of order 0. Their values are $\alpha_2 = 5.520$ and $\alpha_3 = 2.405$. D_T is the thermal diffusivity of the solution. For the present case, we take D_T to be the thermal diffusivity of water, which at 10° is 0.00138 cm$^2 \cdot s^{-1}$. The time constants estimated for thermal relaxation assuming perfect thermal contacts should provide lower limits. When we insert D_T and the length l into Eq. 9, for the case of an ideal cylinder as thick as the sample investigated in our measurements, we obtain $\tau_2 = 2.38$ ms and $\tau_3 = 12.5$ ms. For details see Ref. 6.

The time scale for heat transport in a free-flowing jet can be different due to the continuous renewal of the solution. This has been investigated in detail by us in a very different experiment (THz pump-THz probe), yielding a characteristic exponential rise and decay of temperature with a time constant $\tau_{jet} \approx 35\ \mu s$. In the case of of the water jet, the speed of the jet rather than thermal diffusion or heat transport out of the irradiated area is the time limiting factor. Heating occurs in a small volume, determined by the laser spot sizes (the $1/e^2$ prove diameter is 400 μm thick in the THz-pump THz-probe experiment). The heat is transported via diffusion using the equations mentioned above and by the water flow in the jet. The speed of water flow in the jet amounts to ca. $2.0 \cdot 10^3$ mm$^3/s$. Based on these numbers, we can deduce the time (τ_{jet}), which is required to move one full probe spot size (5400 μm), implying that the water is renewed and equilibrium conditions are reached. Such time is smaller than 400 $\mu m/(\frac{2.0 \cdot 10^3 mm^2/s}{\pi(0.4mm)^2}) \approx 70\ \mu s$.

Similar parameters hold for the water jet used here in optical-pump THz-probe (OPTP) experiments, e.g. the solution is fully replenished in less than 70 μs. Therefore, within the 300 ps time window that is probed in the experiments, any contribution due to heat diffusion can be neglected. Heat transfer cannot explain the observed picosecond time constants reported in this paper.

8 Fluorescence Measurements of HPTS and OPTS

Figure S10 shows the fluorescence spectrum of HPTS at acidic and basic conditions.

9 Long-Time OPTP Signal of HPTS

In Fig. S11, we plot the OPTP $\Delta E/E$ signal for HPTS in the time between 0 and 180 ps on a logarithmic scale. Obviously, the time trace is dominated by a long-term exponential decay attributed to thermalization and indicated here by the blue dashed line. While for MPTS we find a perfect agreement, for HPTS the experimental data deviate from a single exponential fit (blue dashed lines) as indicated by black arrows. In contrast, for MPTS no significant deviations are observed (inset). The black curve corresponds to a fit including

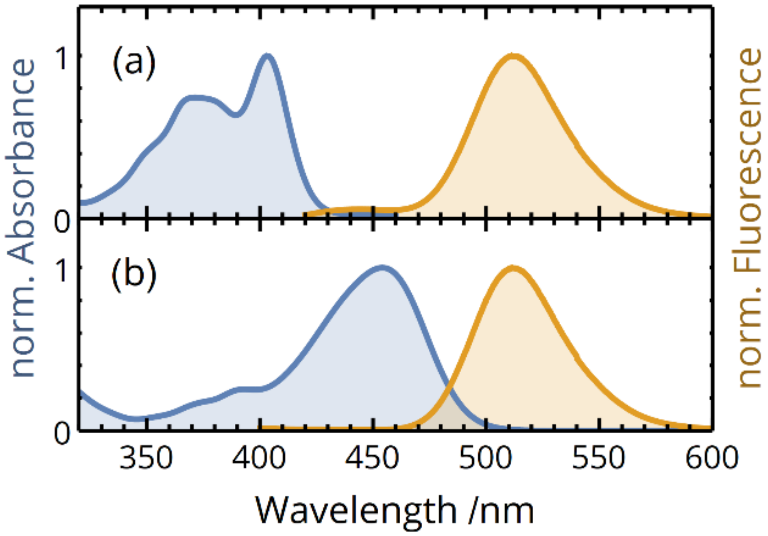

Fig. S10: Normalized absorbance and fluorescence spectra of Pyranine at (a) acidic (λ_{ex} = 400 nm, pH 4) and (b) basic conditions (λ_{ex} = 385 nm). In moderate acidic conditions, the maximum emission is found at 510nm. The origin of this emission is the relaxation of the PyO-* to PyO-. The origin of the emission around 440 nm is the relaxation of undissociated PyOH*. In basic conditions, this emission around 440 nm is not observed since all pyranine molecules are already deprotonated.

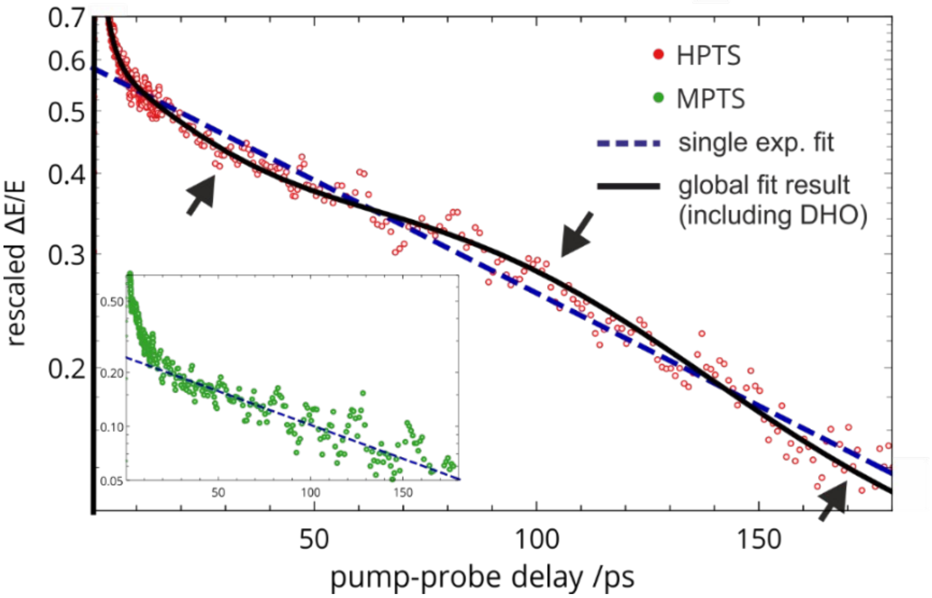

Fig. S11: Logarithmic representation of the HPTS (red) and MPTS transient signals (inset, green). The long-term exponential decay (τ_2), attributed to thermalization, is shown as a blue-dashed line.

an additional damped harmonic oscillation.

We can exclude diffusion-assisted, reversible geminate-recombination of the proton as proposed by Pines and Huppert [7] for a 20 mM concentration as follows: In D_2O, the rates for proton transfer into the solvent (kw) and the back reaction (k_{gem}) are found to be of the same order of magnitude (kw= 245 ps^{-1} and $k_{gem} = 900\ ps^{-1}$), however proton transfer into the solvent network still dominates [8]. Here we propose that, due to the charge, we can follow the propagation into the bulk solvent causing an amplitude modulation in $\Delta E/E$, as similarly reported for bulk water [9–11]. It should be noted that the damping of an acoustic phonon can be described as $exp(-\alpha r)$, with r being the traveling distance and α scales quadratically with the frequency, i.e. $\alpha/\nu^2 = 19 \cdot 10^{-15}\ \mathrm{s}^2/m$ at 30°C [12] which facilitates propagation at low frequencies. at 10 GHz, $\alpha = 1.9 \cdot 10^6\ s^2/m$. Thus, even at a distance of approximately 300Å, the damping amounts to a factor of $exp(\alpha r) = 0.94$. This explains very well the observation over time scales of more than 100 ps.

10 Additional Details of the Experimental Setup

HPTS was obtained from ACROS organics. 8-Methoxypyrene-1,3,6-trisulfonate (MPTS) was synthesized from HPTS following a previously reported route[13]. The water was of ultrapure quality with a measured conductivity of less than 0.055 μS/cm. Sample concentrations were kept at 20 mM. At this concentration no deviation from a highly diluted sample should be expected. In order exclude the possibility that optical excitation of water results in additional artifacts we recorded the OPTP spectrum of bulk water for comparison. No signals can be seen (see Fig. S12).

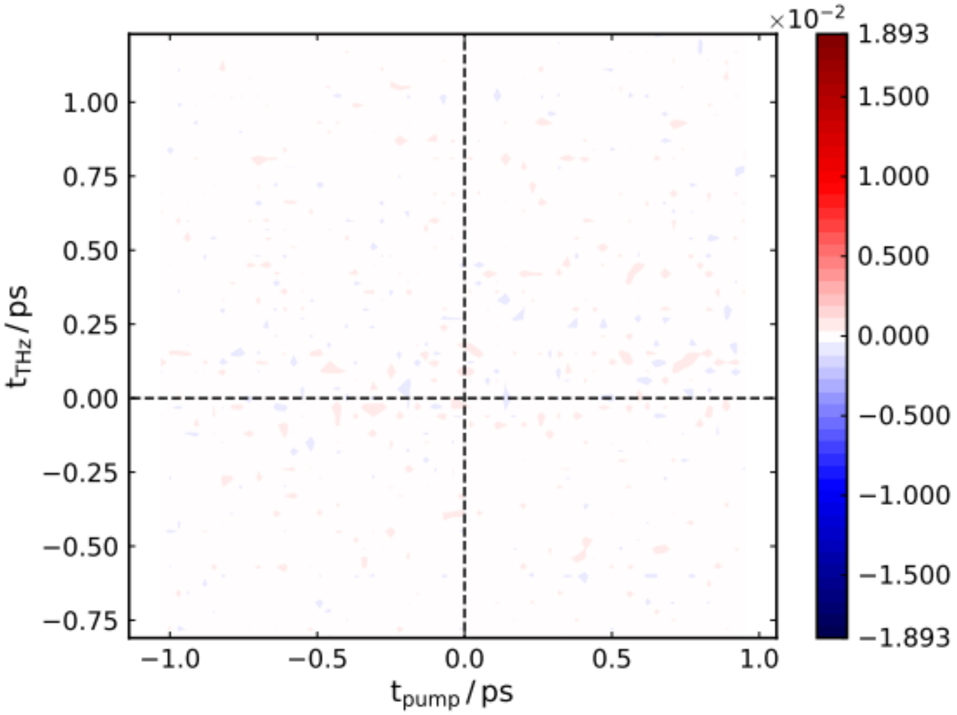

Fig. S12: OPTP measurement of bulk water. The change in THz field is plotted as a function of pump-probe delay. No signal is observed.

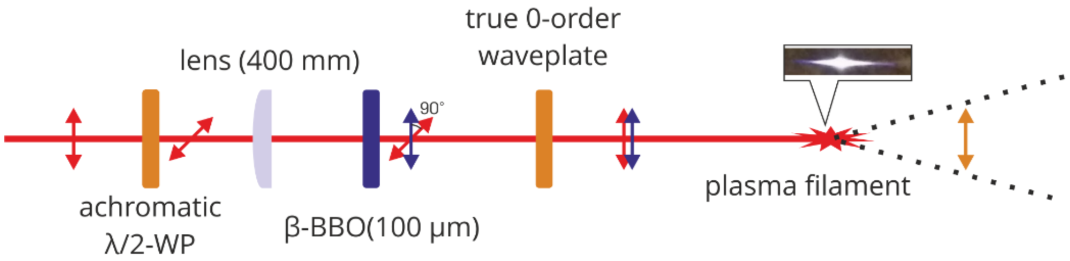

Fig. S13: THz generation by plasma filamentation. The beam is guided through a half-wave plate and then focused by a 40 cm lens through a 100 μm thick beta-BBO crystal. The fundamental beam is vertically polarized, while the second harmonic beam is horizontally polarized. To match both polarizations a true 0-order dual wavelength waveplate rotates the fundamental beam by 90°, while retaining the polarization of the second harmonic beam. In the focus a plasma filament is formed, emitting the final broadband THz beam.

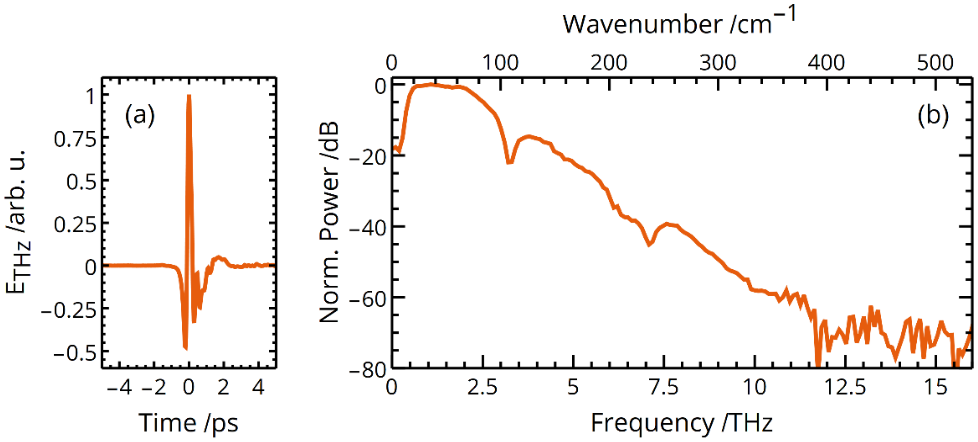

Fig. S14: THz probe pulse waveform (a) and corresponding spectrum (b). Highest intensity is found between 20 − 100 cm^{-1}. The cut-off frequency is around 400 cm^{-1}. The spectral dynamic range is better than 70 dB

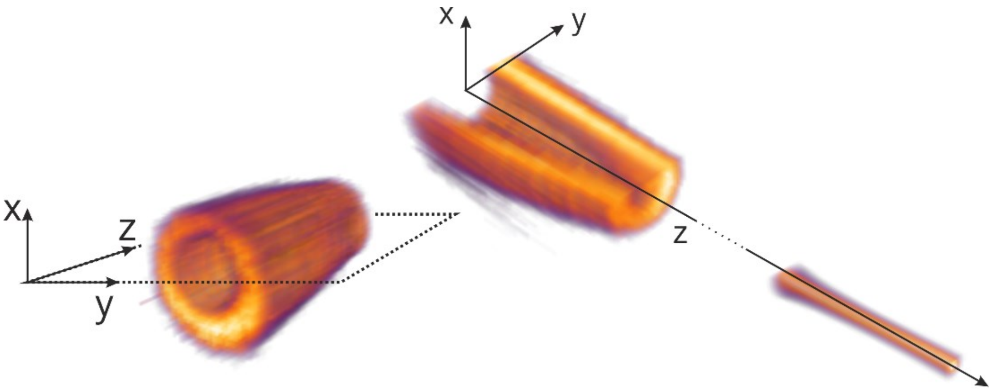

Fig. S15: Three-dimensional THz beam profile at the sample position (recorded with Pyrocam III, Ophir). The THz beam has a conical profile However, at the focus the beam resembles a Gaussian with a beam diameter of 0.64 mm ($1/e^2$).

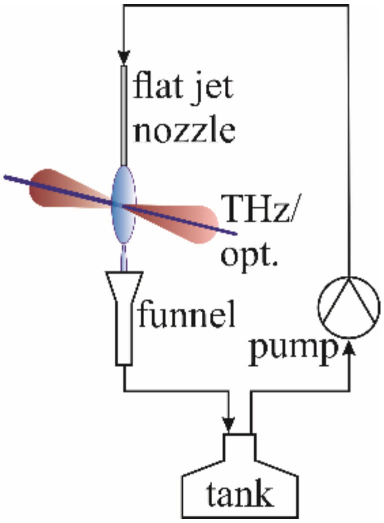

Fig. S16: Setup for the thin-jet apparatus. The solution is pressed through a nozzle by a pump with a pulseless operation design. The solution is collected with a funnel into a reservoir tank. The optical pump beam and the THz probe beam are collinearly aligned into the water jet. The THz probe beam is focused into the center of the flat jet, the optical beam diameter is adjusted to be slightly larger.

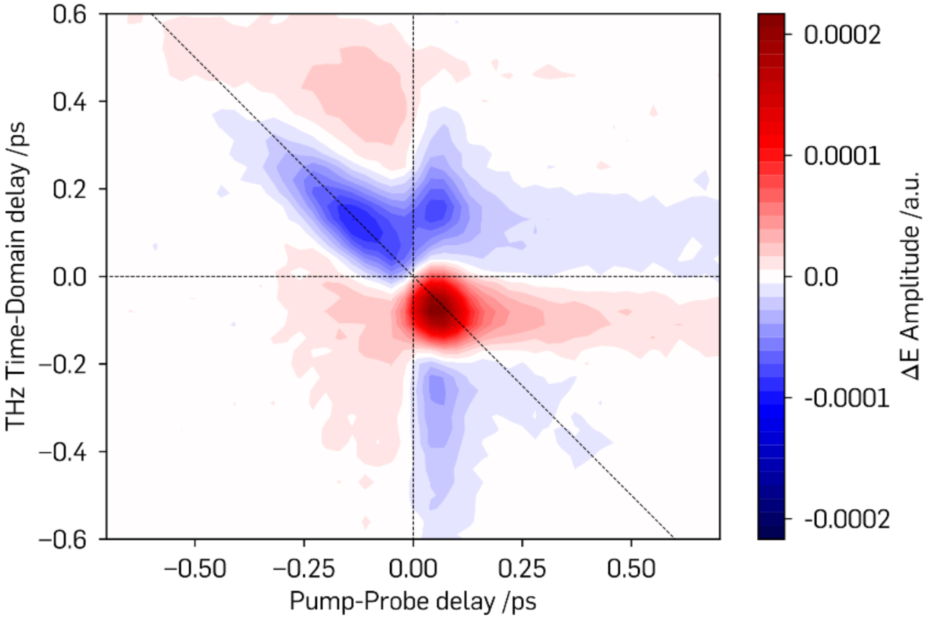

Fig. S17: OPTP measurements of HPTS. The change in THz field is plotted as a function of pump-probe delay around $t = 0$ fs. The THz time-domain axis was scanned using the rapid-scanning technique, while the pump-probe delay was scanned with a linear delay line.

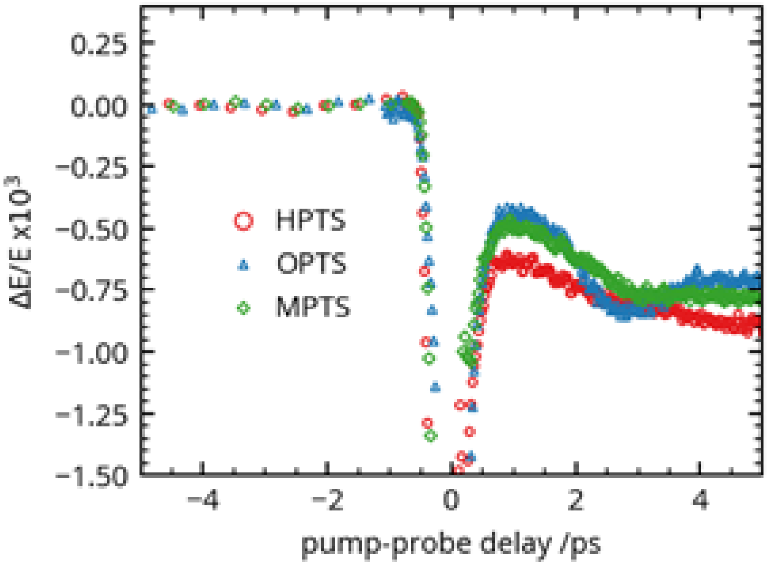

Fig. S18: Negative time signal between -5 ps and +5 ps for HPTS illustrating that there is no signal at negative pump-probe delays (i.e. before the pulse overlap region).

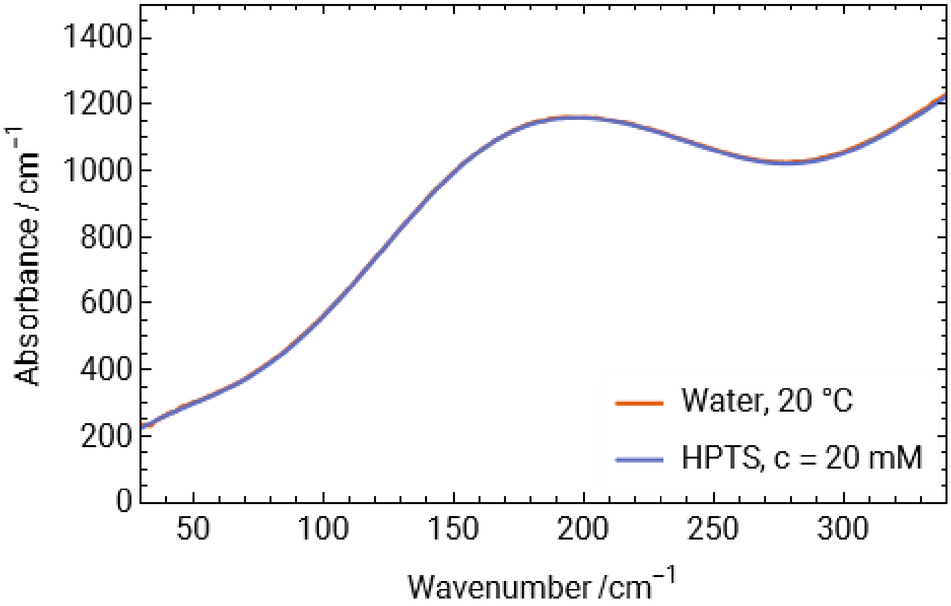

Fig. S19: Comparison of the THz absorption spectrum of HTPS and water as measured by Fourier-Transform Infrared Spectroscopy (Bruker Vertex 80v). The two spectra are essentially overlapping, and no sharp absorption features of the HPTS molecules are observed.

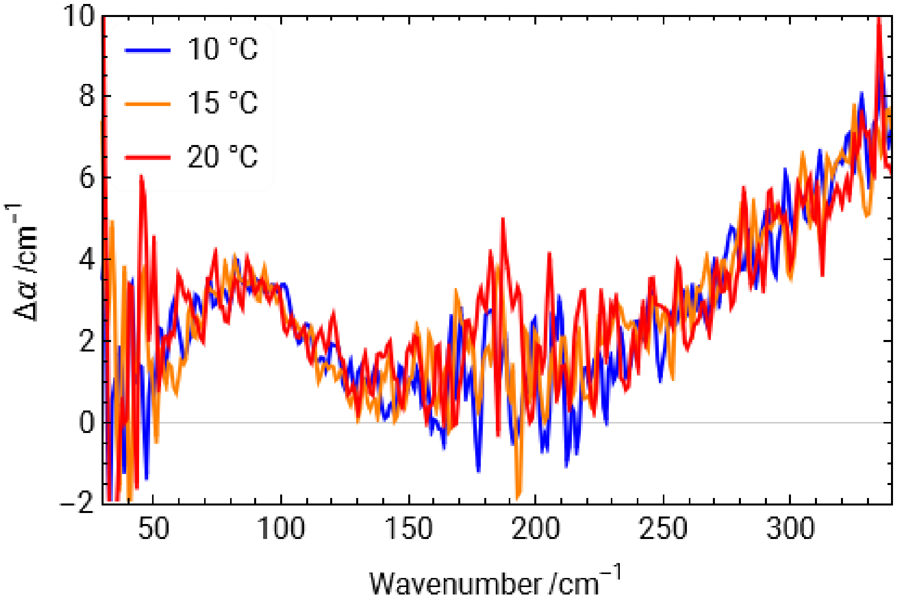

Fig. S20: Difference in absorption between a aqueous HPTS solution (c = 20mM), and pure water at 10 °C, 15 °C, and 20 °C.

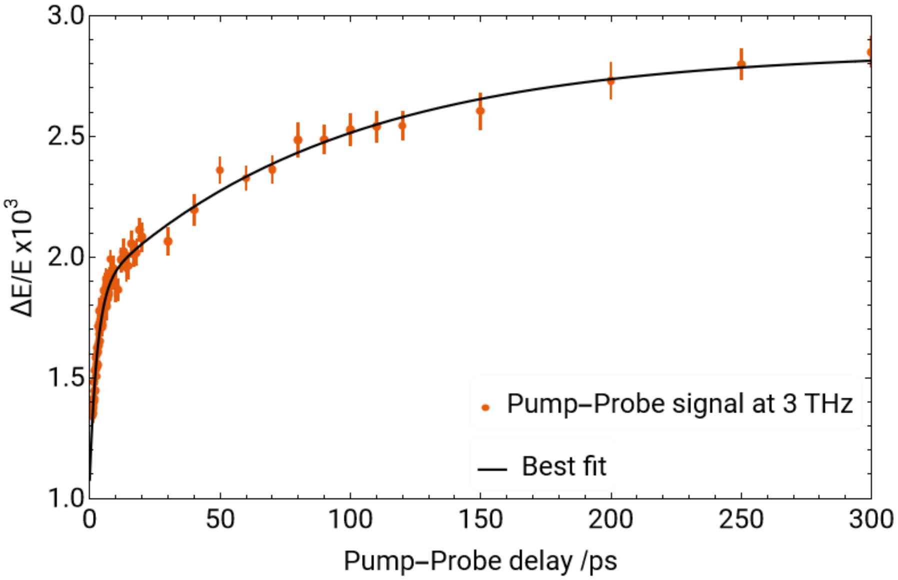

Fig. S21: OPTP signal of HPTS (c = 20 mM) at 3 THz. The data could be fitted with two time constants (biexponential model) of (2.9 ± 0.2) ps and (93 ± 7) ps.

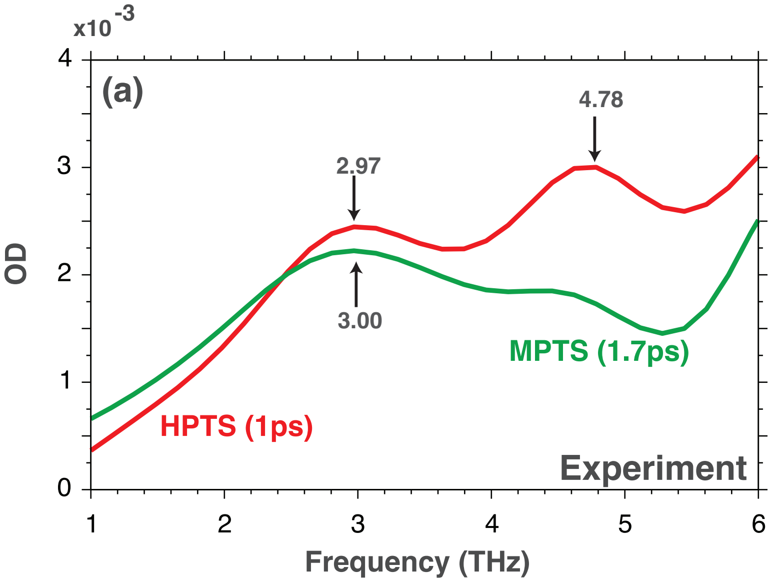

Fig. S22: Frequency resolved OPTP signal of HPTS and MPTS at 1 ps and 1.7 ps respectively. For HPTS there are two maxima at 2.97 THz and 4.78 THz. For MPTS there is one maxima at 3.00 THz.

References

(1) C.-H. Wu, L. J. Karas, H. Ottosson and J. I.-C. Wu, *Proc. Natl. Acad. Sci.*, 2019, **116**, 20303–20308.

(2) C. Cohen-Tannoudji, B. Diu and F. Laloe, *Quantum Mechanics*, 1986, **2**, 626.

(3) *IQmol: The Smart Choice in Molecular Visualization Software*, `http://iqmol.org`, Accessed: 2022-09-12.

(4) H. Liu, Y. Wang and J. M. Bowman, *J. Am. Chem. Soc.*, 2014, **136**, 5888–5891.

(5) H. R. Zelsmann, *J. Mol. Struct.*, 1995, **350**, 95–114.

(6) T. Q. Luong, Y. Xu, E. Bründermann, D. M. Leitner and M. Havenith, *Chem. Phys. Lett.*, 2016, **651**, 1–7.

(7) R. Simkovitch, D. Pines, N. Agmon, E. Pines and D. Huppert, *J. Phys. Chem. B.*, 2016, **120**, 12615–12632.

(8) O. F. Mohammed, D. Pines, E. T. Nibbering and E. Pines, *Angew. Chem. Int. Ed.*, 2007, **119**, 1480–1483.

(9) M. Heyden and D. J. Tobias, *Phys. Rev. Lett.*, 2013, **111**, 218101.

(10) V. Conti Nibali and M. Havenith, *J. Am. Chem. Soc.*, 2014, **136**, 12800–12807.

(11) D. C. Elton and M. Fernández-Serra, *Nat. Commun.*, 2016, **7**, 1–8.

(12) F. Yang, T. Atay, C. Dang, T. Grimsley, S. Che, J. Ma, Q. Zhang, A. Nurmikko and H. Maris, J. Phys. Conf. Ser. 2007, vol. 92, p. 012024.

(13) C. Spies, B. Finkler, N. Acar and G. Jung, *Phys. Chem. Chem. Phys.*, 2013, **15**, 19893–19905.